UC Berkeley
UC Berkeley Previously Published Works

Title
Cyclic steady states of treaded rolling bodies

Permalink
https://escholarship.org/uc/item/89r781t0

Journal
International Journal for Numerical Methods in Engineering, 99(3)

ISSN
0029-5981

Authors
Govindjee, Sanjay
Potter, Trevor
Wilkening, Jon

Publication Date
2014-07-20

DOI
10.1002/nme.4678

Peer reviewed

Cyclic steady states of treaded rolling bodies

Sanjay Govindjee*,†, Trevor Potter and Jon Wilkening

University of California, Berkeley, CA 94720, USA

SUMMARY

The analysis of spinning axisymmetric bodies undergoing finite deformation is useful for understanding the behavior of a wide variety of engineering systems – for example, rolling tires. However, progress beyond the axisymmetric case has been lacking. In this work, we present a methodology for the treatment of treaded rolling bodies by devising a Newton–Krylov shooting scheme for the computation of cyclic steady states of motion. The scheme advocated permits one to determine the entire transient (cyclically steady) motion of a spinning treaded body with consideration of viscoelasticity as well as contact. We demonstrate the viability of the method through three examples, (1) a viscoelastic cylinder with eight sinusoidal tread blocks, (2) a viscoelastic cylinder with 16 square tread blocks, and (3) a viscoelastic oval in which repeated contact and separation from a rigid plane excites distinct transient vibrational modes in the body during each cycle. For practical values of the viscoelastic relaxation time, the new approach is found to converge faster than the naïve approach of evolving an initial guess over many cycles until a cyclic steady state is reached. Copyright © 2014 John Wiley & Sons, Ltd.

1. INTRODUCTION

The analysis of finitely deformable rolling bodies is an important and well-known problem in engineering. In the case where the body (in the reference configuration) is axisymmetric, important early works include Padovan and Paramodilok [1, 2], Oden and Lin [3], Padovan [4], Bass [5], and Kennedy and Padovan [6]. This literature formulates the equations of motion in the frame of reference of an observer translating alongside the rotating body, who measures deformation at a point relative to the location of the material point that would have been there were the body rotating rigidly with constant angular velocity. We will refer to this as the 'lab frame' and the usual reference configuration as the 'material' or 'Lagrangian' frame. The lab frame permits a formulation of the equations of motion that allows for finite deformation elastic and viscoelastic stress analysis of the body while in contact with, say, a rigid plane – for example, a roadway. The solution computed is a true *steady-state* solution; it is purely time-independent in the lab frame.

A major and long-standing shortcoming of this analysis framework is that it strictly requires an axisymmetric reference configuration of the body [7, 8]. Indeed, the material properties and geometry of the body must be invariant under rotation about the cylinder axis for the equations of motion in the lab frame to be independent of time. In particular, for applications where the rolling body has a tread pattern, the framework outlined previously is not applicable because the reference domain in the lab frame would vary in time.

Notwithstanding, if one contemplates the motion of a rolling treaded body, it is apparent that for a wide class of conditions, a *cyclic* steady state will be reached. Consider for example an automobile

---

*Correspondence to: Sanjay Govindjee, University of California, Berkeley, CA 94720, USA.
†E-mail: s_g@berkeley.edu

tire rolling down the road. In principle, for uniform roadways, the state of deformation of the tire will appear the same to an observer moving with the axle *at the instant* that a tread block is in centered contact with the roadway. It matters not which tread block is presently in contact. Furthermore, as the tread block rotates, the tire will undergo a dynamic oscillation that will return to the exact same state once the tread block has rotated through any element of the body's symmetry group. One naïve method for dealing with this issue would be to roll the body (computationally) in a Lagrangian frame from zero velocity up to the desired rolling velocity, and then to wait for the system to settle into the desired cyclic steady state. This brute force approach is certainly valid but can require large computational resources and leaves, as an open question, the difficulty of ensuring that the cyclic steady state has been reached. In the work of Qi *et al.* [9], a second method of treating the treaded body problem is discussed. However, the method described is proprietary, and no detail is provided to allow for a scientific assessment of the procedure. It is the main objective of this work to outline a scheme by which cyclic steady state motions of a rolling body can be computed in the presence of viscoelasticity as well as contact.

In Section 2, we review in detail the geometrical modeling of the problem, the relevant boundary conditions, and the material modeling assumptions. In Section 3, we define our scheme for the determination of cyclic steady solutions. The methodology amounts to finding the zero of an expression that measures the difference between the system's state at the start and end of a (defined) period of motion, under the constraint of a system of partial differential equations representing the evolution of the system. We outline our numerical methods in Section 4, and in Section 5, we demonstrate our scheme on a sequence of examples. In Section 6, we summarize our findings.

2. CONSTITUTIVE EQUATIONS AND BOUNDARY CONDITIONS

2.1. Reference configuration

For simplicity, we will consider two-dimensional treaded bodies, although our methods also apply to three-dimensional problems. To describe a two-dimensional body, we define a reference domain $\mathcal{B}$ with material points $X = (X_1, X_2)$. We work in a Lagrangian frame because the reference domain in the lab frame is not stationary in time. Without treads, the two-dimensional body is an annulus about the origin with inner radius r_1 and outer radius r_2. The reference configuration is then given by the set

$$\mathcal{B} = \{(X_1, X_2) \mid r_1 \leqslant \|X\|_2 \leqslant r_2\} . \tag{2.1}$$

The inner boundary $\Gamma_h = \{X \mid \|X\|_2 = r_1\}$ is called the hub, and the outer boundary $\Gamma_e = \{X \mid \|X\|_2 = r_2\}$ is called the edge.

The aforementioned treadless body can be seen as the image of the set $A = \{(r, \theta) \mid r_1 \leqslant r \leqslant r_2, 0 \leqslant \theta < 2\pi\}$ under the polar coordinate map $P(r, \theta) = (r \cos \theta, r \sin \theta)$. To obtain a body with treads, we perturb $P(r, \theta)$:

$$
\begin{aligned}
P_{\varepsilon,\beta}(r, \theta) &\overset{\text{def}}{=} \psi(r, \varepsilon, \beta)(\cos \theta, \sin \theta) \\
\psi(r, \varepsilon, \beta) &\overset{\text{def}}{=} r + \varepsilon(r - r_1) \cos(\beta\theta) .
\end{aligned}
\tag{2.2}
$$

The integer β is the number of tread blocks, and the parameter ε is the amplitude of the treads relative to the body's size. We then define the reference configuration for the treaded body to be $\mathcal{B}_{\varepsilon,\beta} = P_{\varepsilon,\beta}(A)$ with hub $\Gamma_h = \{P_{\varepsilon,\beta}(r, \theta) \mid r = r_1, 0 \leqslant \theta < 2\pi\}$ and edge $\Gamma_e = \{P_{\varepsilon,\beta}(r, \theta) \mid r = r_2, 0 \leqslant \theta < 2\pi\}$. Figure 1 shows the reference domain for $\beta = 8, \varepsilon = 0.1$. When there is no danger of confusion, we will drop the subscripts from $\mathcal{B}_{\varepsilon,\beta}$ and write $\mathcal{B}$ for the reference configuration. We remark that the methodology described in what follows is not limited to sinusoidal perturbations of $P(r, \theta)$. While most of the paper focuses on $\psi(r, \varepsilon, \beta)$ having the aforementioned form, we consider a discontinuous square-wave perturbation in Section 5.6.
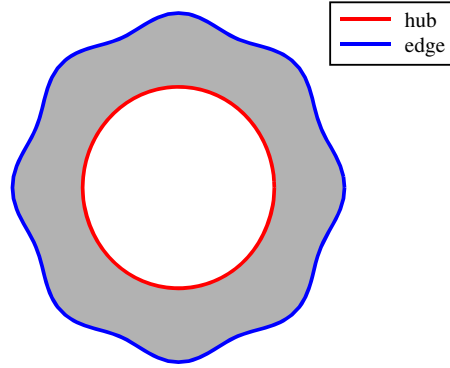
Figure 1. The treaded rolling body corresponding to the reference domain $\mathcal{B}_{0,1,8}$.

2.2. Elastic response

The motion of the body is given by $\boldsymbol{\phi}(X, t)$ with deformation gradient $\mathbf{F} = \partial\boldsymbol{\phi}/\partial X$. Without loss of generality, we assume a plane strain elastic response that is described by a compressible Mooney–Rivlin model, with stored energy function $\boldsymbol{\Psi}_e(I_1, I_2, I_3)$ given in terms of the invariants of the three-dimensional right Cauchy–Green tensor $\mathbf{C}_3 = \begin{bmatrix} \mathbf{C} & 0 \\ 0 & 1 \end{bmatrix}$, where $\mathbf{C} = \mathbf{F}^{\mathrm{T}}\mathbf{F}$:

$$\boldsymbol{\Psi}_e = \frac{\kappa}{4}(I_3 - \log I_3 - 1) + \frac{\mu}{2}(1 - s)(I_1 - \log I_3 - 3) + \frac{\mu}{2}s(I_2 - 2\log I_3 - 3). \quad (2.3)$$

Here, $\kappa > 0$ is the bulk modulus, $\mu > 0$ is the shear modulus, and $s \in [0, 1]$ can be chosen to balance the two shear terms. The energy $\boldsymbol{\Psi}_e$ is polyconvex [10, Section 4.9] and satisfies the conditions for Ball's theory [11] of existence in finite deformation elasticity. The first Piola–Kirchhoff stress tensor $\mathbf{P}_e$ that arises from $\boldsymbol{\Psi}_e$ is

$$\mathbf{P}_e = \frac{\partial\boldsymbol{\Psi}_e}{\partial\mathbf{F}} = \frac{\kappa}{2}(I_3 - 1)\mathbf{F}^{-\mathrm{T}} + \mu(1 - s)\left(\mathbf{F} - \mathbf{F}^{-\mathrm{T}}\right) + \mu s\left(I_1\mathbf{F} - \mathbf{FC} - 2\mathbf{F}^{-\mathrm{T}}\right). \quad (2.4)$$

2.3. Viscoelastic response

Many popular models of viscoelasticity employ linear evolution equations for the (large deformation) viscoelastic stresses, and we have, indeed, successfully applied our methods in this case [12] using a model of Simo [13]. However, it has been demonstrated in [14], by counterexample, that such models can lead to exponential energy growth and thus may not satisfy the 2nd Law of Thermodynamics. Therefore, here, we use the viscoelastic model of Reese and Govindjee [15–17], a nonlinear Sidoroff-class model [18] that has been proven to satisfy the 2nd Law.

The model of Reese and Govindjee [16] is derived by assuming a multiplicative split of the deformation gradient

$$\mathbf{F} = \mathbf{F}_e\mathbf{F}_v \quad (2.5)$$

into an elastic part $\mathbf{F}_e$ and a viscous part $\mathbf{F}_v$. We define a viscoelastic stored energy function $\boldsymbol{\Psi}_v$ that depends only on a deformation measure associated with the so-called elastic part, $\mathbf{b}_e = \mathbf{F}_e\mathbf{F}_e^{\mathrm{T}}$:

$$\boldsymbol{\Psi}_v = \nu\left(\frac{\kappa}{4}\left(I_3^e - \log I_3^e - 1\right) + \frac{\mu}{2}(1 - s)\left(I_1^e - \log I_3^e - 3\right) + \frac{\mu}{2}s\left(I_2^e - 2\log I_3^e - 3\right)\right). \quad (2.6)$$

Here, I_1^e, I_2^e, I_e^e are the invariants of the three-dimensional tensor $\mathbf{b}_{3e} = \begin{bmatrix} \mathbf{b}_e & 0 \\ 0 & 1 \end{bmatrix}$, and ν is a parameter that weights the strength of the viscoelastic response. $\boldsymbol{\Psi}_v$ gives rise to the viscoelastic part of the first Piola–Kirchhoff stress tensor $\mathbf{P}_v$:

$$\mathbf{P}_v = 2\frac{\partial \mathbf{\Psi}_v}{\partial \mathbf{b}_e}\mathbf{b}_e \mathbf{F}^{-T}$$

$$= v\left(\frac{\kappa}{2}(I_3^e - 1)\mathbf{I} + \mu(1-s)(\mathbf{b}_e - \mathbf{I}) + \mu s\left(I_1^e \mathbf{b}_e - \mathbf{b}_e^2 - 2\mathbf{I}\right)\right)\mathbf{F}^{-T}. \tag{2.7}$$

In order to have a closed system, the dynamics of the internal variable $\mathbf{b}_e$ must be specified:

$$\dot{\mathbf{b}}_e = \boldsymbol{\ell}\mathbf{b}_e + \mathbf{b}_e\boldsymbol{\ell}^T - 2\mathcal{V}(\boldsymbol{\tau}_v)\mathbf{b}_e, \tag{2.8}$$

where

$$\boldsymbol{\ell} = \dot{\mathbf{F}}\mathbf{F}^{-1}, \qquad \boldsymbol{\tau}_v = 2\frac{\partial \mathbf{\Psi}_v}{\partial \mathbf{b}_e}\mathbf{b}_e$$

$$\mathcal{V}(\boldsymbol{\tau}_v) = \frac{1}{2\mu\tau}\left(\boldsymbol{\tau}_v - \frac{1}{2}(\text{tr}\,\boldsymbol{\tau}_v)\mathbf{I}\right) + \frac{1}{4\kappa\tau}(\text{tr}\,\boldsymbol{\tau}_v)\mathbf{I}. \tag{2.9}$$

Note that τ is a viscoelastic relaxation time parameter, while $\boldsymbol{\tau}_v$ is the Kirchhoff stress tensor corresponding to $\mathbf{P}_v$.

Finally, we define the total first Piola–Kirchhoff stress tensor to be the sum of the elastic and viscoelastic stress tensors:

$$\mathbf{P} = \mathbf{P}_e + \mathbf{P}_v. \tag{2.10}$$

Assuming constant Dirichlet or Neumann boundary conditions, a computation shows that the total stored energy function $\mathbf{\Psi} = \mathbf{\Psi}_e + \mathbf{\Psi}_v$ satisfies the 2nd Law of Thermodynamics and may be used to construct a Lyapunov function of the dynamical system.

2.4. Boundary conditions

We imagine the body is being spun at a constant speed ω along the hub so that

$$\boldsymbol{\phi}(X,t) = \mathbf{R}(t)X \text{ on } \Gamma_h, \tag{2.11}$$

where $\mathbf{R}(t)$ is the rotation matrix given by $\begin{bmatrix} \cos(\omega t) & -\sin(\omega t) \\ \sin(\omega t) & \cos(\omega t) \end{bmatrix}$. On the edge, either there is a free surface or the body is in contact with, say, a roadway (or other stiff surface). The free surface is described by the absence of traction along that part of the boundary of the reference configuration. It is given by the formula $\mathbf{PN} = \mathbf{0}$.

We model contact with the road by prescribing a simple penalty force pushing against the edge of the body whenever the edge penetrates beneath the surface of the road (Figure 2). More specifically, let $h > r_1$ be the distance from the x-axis to the road, so that the road is lying along $y = -h$. If X is a point on the edge and $x_2 = \boldsymbol{\phi}_2 = \boldsymbol{\phi}_2(X) < -h$, we consider a force of magnitude $k\gamma(-h - x_2)$ per unit reference area in the x_2 direction, $\mathbf{e}_2$. We require that $\gamma(0) = 0$ and that $\gamma(z)$ is monotonically increasing for $z > 0$. The parameter $k > 0$ controls the road stiffness. The specific choice of γ will be discussed in Section 5. The traction force is applied at the point $x = \boldsymbol{\phi}(X)$ in the deformed configuration. In precise terms, at a point X on the edge with outward normal $\mathbf{N}$ of the reference configuration, we have

$$\mathbf{PN} = k\gamma(-h - x_2)\mathbf{e}_2. \tag{2.12}$$

The free boundary condition and the road boundary condition on the edge can both be expressed via (2.12) by choosing γ such that $\gamma(z) = 0$ for $z \leqslant 0$. For later convenience, we define

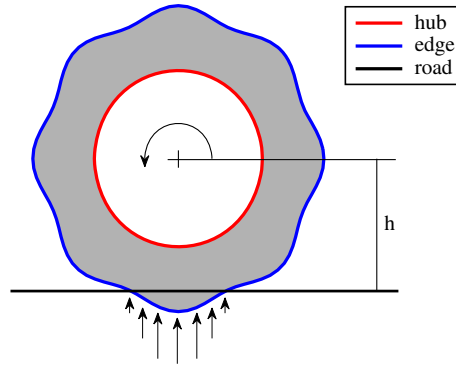$$\mathbf{h} = k\gamma(-h - x_2)\mathbf{e}_2. \tag{2.13}$$

Figure 2. Illustration of the positioning of the road and the traction forces experienced on the edge. The traction increases in magnitude the deeper the body penetrates the road. The direction of rotation is also indicated.

2.5. Equations of motion

The motion is given by

$$\begin{aligned}
\rho_R \ddot{\boldsymbol{\phi}} &= \mathrm{DIV}\,\mathbf{P} && \text{on } \mathcal{B} \\
\dot{\mathbf{b}}_e &= \boldsymbol{\ell}\mathbf{b}_e + \mathbf{b}_e\boldsymbol{\ell}^{\mathrm{T}} - 2\mathcal{V}(\boldsymbol{\tau}_v)\mathbf{b}_e && \text{on } \mathcal{B},
\end{aligned} \tag{2.14}$$

with boundary conditions

$$\begin{aligned}
\boldsymbol{\phi}(X,t) &= \mathbf{R}(t)X && \text{on } \Gamma_h \\
\mathbf{PN} &= \mathbf{h} && \text{on } \Gamma_e .
\end{aligned} \tag{2.15}$$

We reduce the second-order equation to a system of first-order equations by introducing the velocity of the motion, $\boldsymbol{v}(X,t)$, as an independent field variable. The equations of motion on $\mathcal{B}$ then become

$$\begin{aligned}
\dot{\boldsymbol{\phi}} &= \boldsymbol{v} \\
\dot{\boldsymbol{v}} &= \frac{1}{\rho_R}\mathrm{DIV}\,\mathbf{P} \\
\dot{\mathbf{b}}_e &= \boldsymbol{\ell}\mathbf{b}_e + \mathbf{b}_e\boldsymbol{\ell}^{\mathrm{T}} - 2\mathcal{V}(\boldsymbol{\tau}_v)\mathbf{b}_e ,
\end{aligned} \tag{2.16}$$

with boundary conditions

$$\begin{aligned}
\boldsymbol{\phi}(X,t) &= \mathbf{R}(t)X && \text{on } \Gamma_h \\
\boldsymbol{v}(X,t) &= \dot{\mathbf{R}}(t)X && \text{on } \Gamma_h \\
\mathbf{PN} &= \mathbf{h} && \text{on } \Gamma_e .
\end{aligned} \tag{2.17}$$

The weak formulation of the equations of motion, which we will need later for finite element analysis, is

$$\begin{aligned}
\int_{\mathcal{B}} \dot{\boldsymbol{\phi}} \cdot \zeta &= \int_{\mathcal{B}} \boldsymbol{v} \cdot \zeta \\
\int_{\mathcal{B}} \dot{\boldsymbol{v}} \cdot \eta &= \int_{\mathcal{B}} -\frac{1}{\rho_R}\mathbf{P} : D\eta + \int_{\Gamma_e} \frac{1}{\rho_R}\mathbf{h} \cdot \eta \\
\int_{\mathcal{B}} \dot{\mathbf{b}}_e : K &= \int_{\mathcal{B}} \left(\boldsymbol{\ell}\mathbf{b}_e + \mathbf{b}_e\boldsymbol{\ell}^{\mathrm{T}} - 2\mathcal{V}(\boldsymbol{\tau}_v)\mathbf{b}_e\right) : K .
\end{aligned} \tag{2.18}$$

Here, ζ, η and K are arbitrary test functions, with K being symmetric tensor-valued. We take the test functions ζ and η to be $\mathbf{0}$ on the hub, Γ_h. When convenient, we will denote the triple $(\boldsymbol{\phi}, \boldsymbol{v}, \mathbf{b}_e)$ by $\mathbf{z}$.

2.6. Linearization

We will need the linearization of the weak form equations, in order to apply Newton's method. We will use the following notation: given a function f of $\mathbf{z}$ and a tangent $\hat{\mathbf{z}}$, we denote the derivative of $f(\mathbf{z})$ in the direction of $\hat{\mathbf{z}}$ as $\widehat{f}$. Precisely,

$$\widehat{f} \stackrel{\text{def}}{=} \frac{d}{d\varepsilon}\bigg|_{\varepsilon=0} f(\mathbf{z} + \varepsilon\hat{\mathbf{z}}). \tag{2.19}$$

With this notation, the linearized weak form equations become

$$\int_{\mathcal{B}} \widehat{\dot{\boldsymbol{\phi}}} \cdot \zeta = \int_{\mathcal{B}} \widehat{\boldsymbol{\nu}} \cdot \zeta$$

$$\int_{\mathcal{B}} \widehat{\dot{\boldsymbol{\nu}}} \cdot \eta = \int_{\mathcal{B}} -\frac{1}{\rho_R}\widehat{\mathbf{P}} : D\eta + \int_{\Gamma_e} \frac{1}{\rho_R}\widehat{\mathbf{h}} \cdot \eta \tag{2.20}$$

$$\int_{\mathcal{B}} \widehat{\dot{\mathbf{b}}_e} : K = \int_{\mathcal{B}} \left(\widehat{\boldsymbol{\ell}\mathbf{b}_e} + \widehat{\mathbf{b}_e\boldsymbol{\ell}^{\mathrm{T}}} - 2\widehat{\mathcal{V}(\boldsymbol{\tau}_v)\mathbf{b}_e} \right) : K.$$

with boundary conditions $\widehat{\dot{\boldsymbol{\phi}}} = \widehat{\boldsymbol{\nu}} = \mathbf{0}$ on Γ_h. See Appendix A for a detailed computation of the terms $\widehat{\mathbf{P}}, \widehat{\dot{\mathbf{b}}_e}$, and $\widehat{\mathbf{h}}$.

3. CYCLIC STEADY STATES

With the equations of motion in hand, we turn to finding cyclic steady states of the treaded body. Other systems in which time-periodic solutions of partial differential equations are of interest include Couette turbulence [19], integrable equations [20], mode-locked lasers [21], and surface water waves [22]. In what follows, we adopt a similar mathematical framework as in these works.

We seek solutions of (2.18) that return to the same state as their initial configuration after some time T. This corresponds (Figure 3) to searching for a solution $\mathbf{z} = (\boldsymbol{\phi}, \boldsymbol{\nu}, \mathbf{b}_e)$ that satisfies

$$\boldsymbol{\phi}\left(\mathbf{R}^{\mathrm{T}}(T)X, T\right) = \boldsymbol{\phi}(X, 0)$$
$$\boldsymbol{\nu}\left(\mathbf{R}^{\mathrm{T}}(T)X, T\right) = \boldsymbol{\nu}(X, 0) \tag{3.1}$$
$$\mathbf{b}_e\left(\mathbf{R}^{\mathrm{T}}(T)X, T\right) = \mathbf{b}_e(X, 0).$$
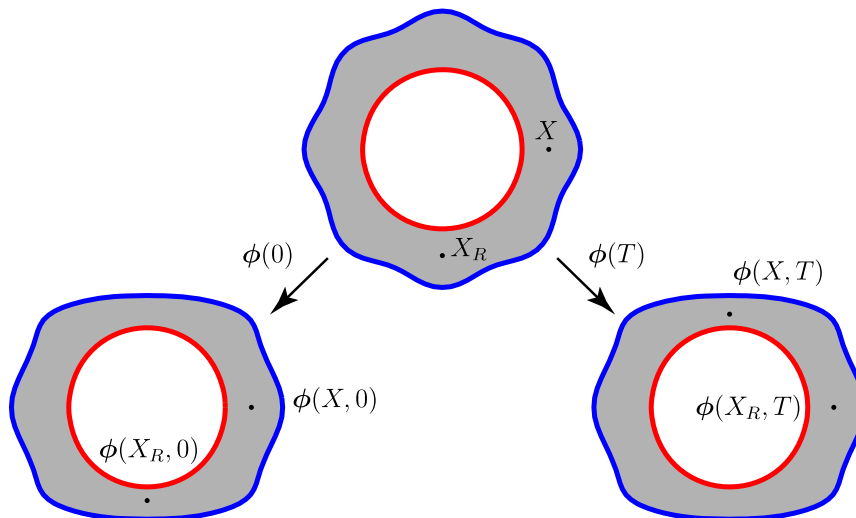

Figure 3. The top figure is the reference configuration with material points X and $X_R = \mathbf{R}^{\mathrm{T}}(T)X$. Bottom left is the deformed configuration at time 0. Bottom right is the deformed configuration at time T, for which the body is in the same state as at time 0. We observe that $\boldsymbol{\phi}(X_R, T) = \boldsymbol{\phi}(X, 0)$.

For a body with no treads, the previous equations make sense for any value of T, and by solving them for all T simultaneously, one would obtain the steady rolling state of the body. This cannot be carried out for a treaded body, because T must be an integer multiple of $2\pi/(\omega\beta)$, where β is the number of tread blocks. In this case, we refer to a solution of (3.1) as a cyclic steady state. In general, one may expect to find different dynamics for different choices of T, but in the viscoelastic case, we observe a single cyclic steady state for any admissible choice of T.

We rewrite Equation (3.1) as a function of an initial condition $\mathbf{z}_0 = (\boldsymbol{\phi}_0, \boldsymbol{\nu}_0, (\mathbf{b}_e)_0)$:

$$\mathcal{H}_T(\mathbf{z}_0) = \mathbf{z}\left(\mathbf{R}^{\mathrm{T}}(T)X, T\right) - \mathbf{z}_0\,, \tag{3.2}$$

where $\mathbf{z}(X, t)$ evolves according to (2.18) with initial condition $\mathbf{z}_0$. We can now search for cyclic steady states by finding a solution to $\mathcal{H}_T(\mathbf{z}_0) = \mathbf{0}$. To find a $\mathbf{0}$ of $\mathcal{H}_T$, we will also require its derivative:

$$D\mathcal{H}_T[\mathbf{z}_0](\hat{\mathbf{z}}_0) = \hat{\mathbf{z}}\left(\mathbf{R}^{\mathrm{T}}(T)X, T\right) - \hat{\mathbf{z}}_0\,, \tag{3.3}$$

where $\hat{\mathbf{z}}(X, t)$ evolves according to the linearized equations (2.20) with initial condition $\hat{\mathbf{z}}_0$.

4. NUMERICAL METHODS

We now describe the numerical methods employed to discretize and then solve $\mathcal{H}_T(\mathbf{z}_0) = \mathbf{0}$. We employ quartic quadrilateral C_0 iso-geometric elements to discretize the weak equations as in Figure 4. We use a structured mesh that is mapped to the reference configuration via $P_{\varepsilon,\beta}$. The numerical degrees of freedom are given by the coefficients of the finite element basis functions used to represent $\boldsymbol{\phi}$, $\boldsymbol{\nu}$, and $\mathbf{b}_e$. The requisite mass matrix solves are performed iteratively using conjugate gradients, which typically converges in 50 iterations, independent of problem size. We evolve the discretized equations in time using a fifth- or eighth-order explicit Runge–Kutta method, both due to Dormand and Prince [23–25].

We chose to use high-order iso-geometric elements to obtain more spatial accuracy relative to the number of degrees of freedom on the mesh. Nothing in our method prevents us from using lower-order approximations; in fact, we have carried out experiments using bi-linear elements on non-smooth structures (Section 5.6). We chose an explicit time stepping scheme to avoid solving nonlinear equations at every time step. This comes at the cost of small time steps needed to resolve compression waves. The fifth- and eighth-order Dormand/Prince schemes have larger stability regions than lower-order explicit methods, which largely offsets any disadvantage of having 6 and 12 internal stages, respectively. The stability regions of the fifth- and eighth-order methods are similar in size, making the eighth-order method roughly twice as expensive as the fifth-order method
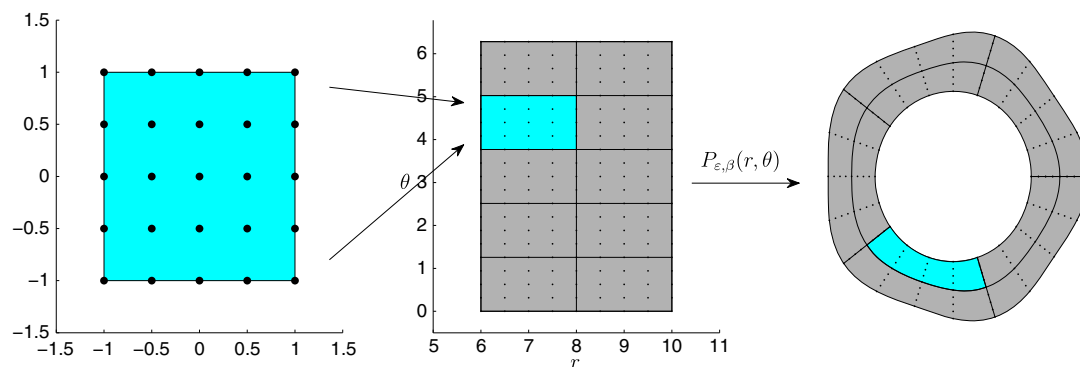

Figure 4. The reference element is mapped to the r-θ plane, where it is then mapped by $P_{\varepsilon,\beta}$ onto the reference configuration $\mathcal{B}_{\varepsilon,\beta}$.

when run with a timestep just small enough to achieve stability; however, at that point, the eighth-order method is several orders of magnitude more accurate at evolving the discrete equations, at least for smooth tread patterns $\psi(r, \varepsilon, \beta)$ and road force functions $\gamma(x)$. Both timestepping schemes proved successful in all the test problems reported below.

With the aforementioned numerical techniques, we can compute $\mathbf{z}(X, T)$ given an initial condition $\mathbf{z}_0$. But to discretize $\mathcal{H}_T$, we must compute $\mathbf{z}(\mathbf{R}^\mathrm{T} X, T)$. We choose the number of elements in the circumferential direction, e_c, to be a multiple of β, the number of tread blocks. This allows us to compute $\mathbf{z}(\mathbf{R}^\mathrm{T} X, T)$ by shifting the values of $\mathbf{z}(X, T)$ at the nodes. Specifically, if after time T the body has rotated over n tread blocks, we shift the values at the nodes by $n e_c / \beta$ elements counterclockwise.

We denote the discretization of $\mathcal{H}_T$ by $\bar{\mathcal{H}}_T$ and denote its derivative, taken about a point $\mathbf{z}_0$, by $D\bar{\mathcal{H}}_T[\mathbf{z}_0]$. $\bar{\mathcal{H}}_T = \mathbf{0}$ is solved using Newton's method. Assuming a solution $\mathbf{z}_0^{(*)}$ that satisfies $\bar{\mathcal{H}}_T(\mathbf{z}_0^{(*)}) = \mathbf{0}$ and a first approximation to $\mathbf{z}_0^{(*)}$, denoted $\mathbf{z}_0^{(0)}$, Newton's method produces successive approximations $\mathbf{z}_0^{(i)}$ by the following procedure:

$$
\begin{aligned}
\text{Solve} \quad & D\bar{\mathcal{H}}_T\left[\mathbf{z}_0^{(i)}\right]\left(\hat{\mathbf{z}}_0^{(i)}\right) = -\bar{\mathcal{H}}_T\left(\mathbf{z}_0^{(i)}\right) \quad \text{for } \hat{\mathbf{z}}_0^{(i)}. \\
\text{Set} \quad & \mathbf{z}_0^{(i+1)} = \mathbf{z}_0^{(i)} + \hat{\mathbf{z}}_0^{(i)}.
\end{aligned}
\tag{4.1}
$$

To solve for $\hat{\mathbf{z}}_0^{(i)}$ in (4.1), we employ the generalized minimal residual method (GMRES), which finds an approximate solution to the linear equation $Ax = b$ iteratively, using only matrix-vector products. See [26] for an introduction to this and other Newton–Krylov methods. We choose this approach over a direct solve, which we implemented but found expensive. Indeed, forming the matrix corresponding to $D\bar{\mathcal{H}}_T\left[\mathbf{z}_0^{(i)}\right]$ is an $\mathcal{O}(n^2 k)$ operation, and directly solving it is an order $\mathcal{O}(n^3)$ operation, where n is the number of spatial degrees of freedom and k is the number of time steps. By contrast, the GMRES algorithm is $\mathcal{O}(n(k + m)m)$, where m is the number of GMRES iterations performed (typically 12). In either approach, the constants in the operation counts involving k are quite large because of the number of internal Runge–Kutta stages and the use of conjugate gradients on the mass matrix.

We now briefly describe the GMRES algorithm applied to our Newton procedure (4.1). We compute an orthonormal basis for span$\{b, Ab, A^2 b, \ldots, A^m b\}$ with $A = D\bar{\mathcal{H}}_T\left[\mathbf{z}_0^{(i)}\right]$ and $b = -\bar{\mathcal{H}}_T(\mathbf{z}_0^{(i)})$. The minimizer of the residual $\|Ax - b\|_2$ over this subspace gives the approximate solution to the linear system, which we set to be $\hat{\mathbf{z}}_0^{(i)}$. To compute a basis for span$\{b, Ab, A^2 b, \ldots, A^m b\}$, we must apply the operator $D\bar{\mathcal{H}}_T[\mathbf{z}_0^{(i)}]$ to multiple inputs. Specifically, we first compute the solution $\mathbf{z}(X, t)$ of the nonlinear equation (2.18) with initial condition $\mathbf{z}_0^{(i)}$ and then evolve the equations linearized about $\mathbf{z}$, (2.20), for multiple initial conditions, that is, those that arise when forming the Krylov vectors. Because the values of $\mathbf{z}(X, t)$ are needed to evolve the linearized equations, the values of $\mathbf{z}(X, t)$ are stored for all time steps and interpolated (to fifth- or eighth-order [23]) as needed by the Runge–Kutta time-stepper for the linearized equations. Alternatively, one can avoid interpolation by re-evolving the nonlinear equations along with the linearized ones [22].

5. RESULTS

5.1. Units and constants

Our choice of units is Newtons (N), megagrams (Mg), and seconds (s). This choice implies the unit for length is millimeters (mm). In the remainder of the results section, we will use the following values for constants, unless otherwise noted. The body has inner radius $r_1 = 240$ mm and outer radius $r_2 = 400$ mm. The density of the body is $\rho = 1 \times 10^{-9}$ Mg/mm^3. The bulk modulus κ and shear modulus μ are 689 N/mm^2 and 6.89 N/mm^2, respectively. The dimensionless viscous strength parameter ν has value 1, and the relaxation time is 0.01 s. The parameter s in the Mooney-Rivlin model is taken as $1/2$. The distance from the axis to the road, h, is 380 mm and the road stiffness

parameter k is 1000 N/mm^2. The body's tread amplitude parameter ε is 0.1, and the number of treads β is 8.

We must also define the road force function $\gamma(x)$, which should be monotonically increasing for $x > 0$ and satisfy $\gamma(x) = 0$ for $x \leqslant 0$. A simple choice would be

$$\begin{cases} \gamma(x) = 0, & x \leqslant 0 \\ \gamma(x) = x, & x \geqslant 0. \end{cases} \tag{5.1}$$

However, this choice of γ is not smooth and will lead to non-smooth discretized equations. Instead, we choose the smooth function

$$\begin{cases} \gamma(x) = 0, & x \leqslant 0 \\ \gamma(x) = \exp(x - x^{-1}), & x \geqslant 0. \end{cases} \tag{5.2}$$

This function has the drawback of converging to zero exponentially fast as $x \to 0$ from the right, resulting in a weak road force for small road penetration. This trade-off between smoothness and enforcement of constraints arises frequently in contact problems.

5.2. Example computation of a cyclic steady state

Figures 5–9 show the results of a typical computation of a cyclic steady state of a treaded body. The mesh size is $e_c = 32$, $e_r = 4$. The body has $\beta = 8$ treads and is rotating with frequency $\omega = 10$ rad/s. We rotate the body over one tread block, which implies $T = 2\pi/(\beta\omega)$.

We take 10000 time steps to evolve the weak equations and the linearized weak equations. This number is chosen to be big enough that the time stepping remains stable. We have found that with
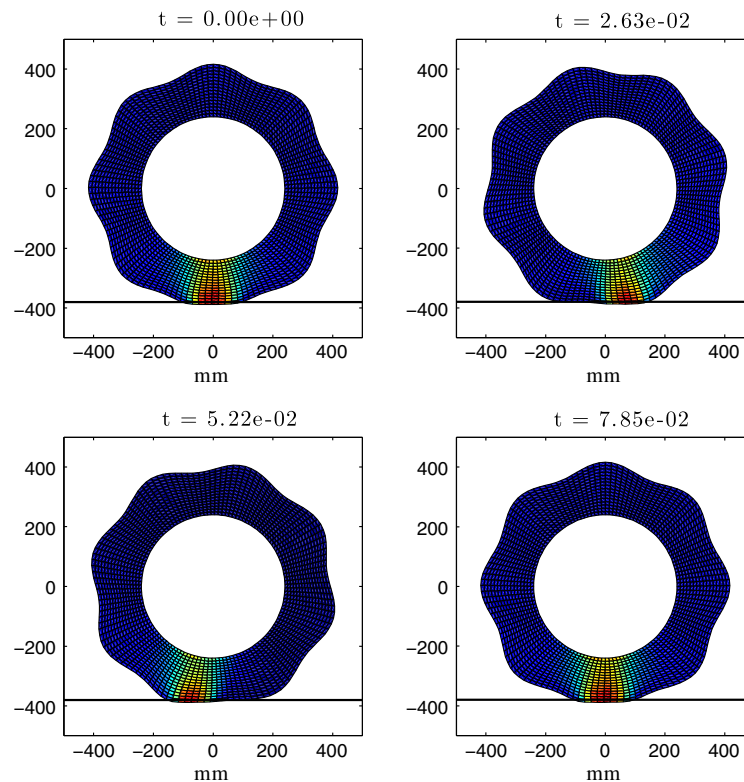

Figure 5. Plot of the body as it rotates counterclockwise from one tread to the next. Red indicates high first principal stress, while blue indicates low first principal stress.
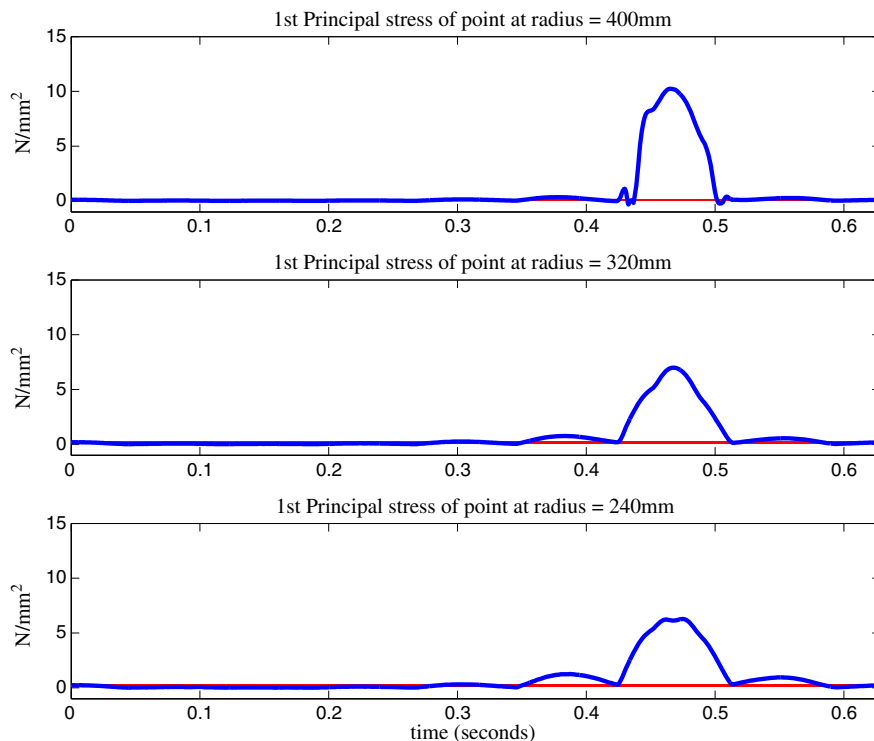
Figure 6. Plots of the evolution of the first principal stress over one revolution. The plots represent points at different distances from the hub, from furthest to closest. The constant lines indicate the initial and final values in each plot, which are equal because of time-periodicity.

the eighth-order method, the number of timesteps required for stability is also sufficient to ensure that the temporal discretization is *fully converged*.

We first perform a static calculation to determine the deformation of the body at rest when pressed against the road. This is used as an initial guess for Newton's method, which solves the cyclic steady-state equations for the rotating body to approximately eight digits of accuracy. Within each Newton iteration, GMRES performs linear solves on the Jacobian of $\bar{\mathcal{H}}_T$. Setting the tolerance on the GMRES residual to $\delta = 10^{-3}$, where we require $\|b - Ax\| < \delta\|b\|$ when approximately solving $Ax = b$, is sufficient for Newton's method to perform well, as shown in Section 5.4. A typical number of GMRES iterations for this tolerance is 12, and a typical number of Newton iterations is 5. The GMRES algorithm dominates the computation. Each iteration requires approximately 15 min on 32 processors; hence, the entire simulation requires approximately $15 \times 5 \times 12$ min $= 15$ h. It is also possible to incrementally increase the road strength, rotation speed, or tread amplitude until the desired values are reached, but we found this unnecessary in the above computation.

5.3. Time evolution of stress of the treaded body

After computing a cyclic steady state for the treaded body, we compute the first principal stress. Figure 5 shows the principal stress of the body at various points in time over a full rotation, while Figure 6 shows the first principal stresses at a material point as it makes one full revolution around the body. At time $t = 0$, the material point begins on the positive x-axis. The first principal stress spikes as the material point passes near the road, and is the largest at the outer boundary of the body where contact with the road is made. We note that the slight double peak in the first principal stress for a material point on the hub occurs because of high shear stresses on either side of the portion of the hub closest to the road. It is to be observed that the solutions found correspond to the cyclic steady state – the starting and ending values at $t = 0$ and $t = 2\pi/\omega$ are identical.

Figure 7 quantifies the difference in stresses at different points along a tread. The first principal stress decreases as we move from the tread crest to the tread trough. At the trough, it is appreciable in size when one of or both the adjacent tread crests are in contact with the road (approximately during the time interval $0.27 < t < 0.58$ in the bottom plot in Figure 7). This is caused by the tread trough being squeezed by the adjacent treads because of its concave geometry.

We also plot the magnitude of the traction experienced by a material point along the edge as it rotates with the body in Figure 8. As might be expected, the traction is the largest at the tread peak and the smallest at the tread trough when the point passes over the road.

In Figure 9, we observe the shear stress along the hub, specifically $\mathbf{PN} \cdot \mathbf{t}$, where $\mathbf{N}$ is the outward normal pointing into the hub and $\mathbf{t}$ is the tangent vector along the hub in the counterclockwise direction. This figure indicates that the largest shear stresses on the hub occur radially inline with the tread troughs.

5.4. Comparison with other methods

To give perspective on the computational cost of our method, we compare it against two commonly used methods: (1) time-independent steady-state computation and (2) evolving the body in time until it reaches a cyclic steady state due to damping. We will refer to our method as method (3). Because method (1) is only applicable to axisymmetric bodies, we apply all three methods to such a body. Our method, however, requires the specification of a period, T. In the case of an axisymmetric body, any value of T will work. For the following examples, we have arbitrarily selected $T = 2\pi/8\omega$, which is the $\varepsilon = 0$ limit of the geometry studied in Section 5.2. We also utilize a quartic mesh size of $e_c = 16$, $e_r = 2$. Aside from these points, the parameters are the same as in Section 5.2.
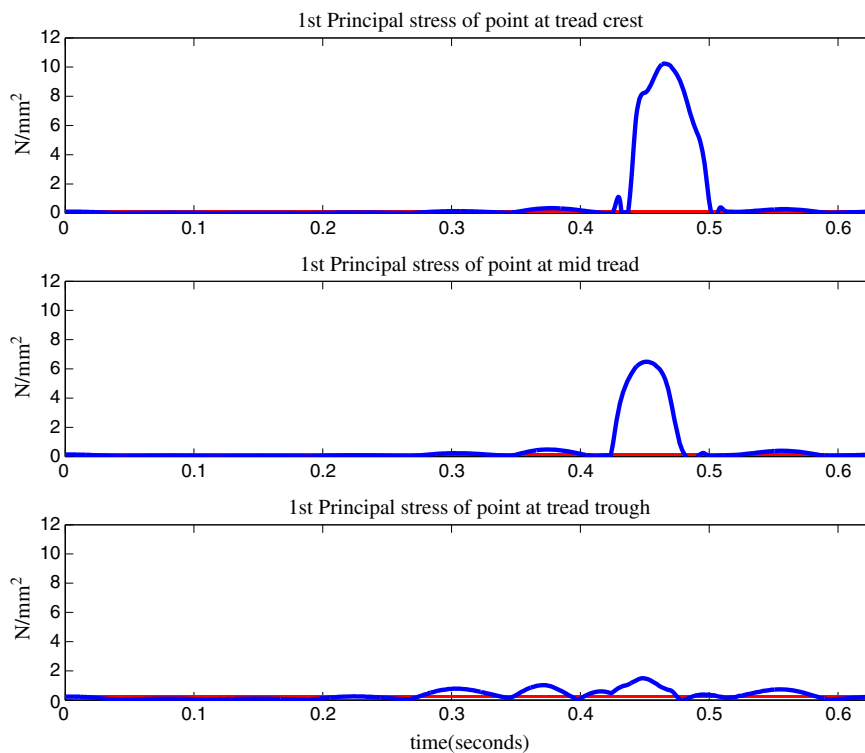

Figure 7. Plots of the evolution of the first principal stress over one revolution. The plots represent points at different locations along the edge of the body. The top plot is at a tread peak, the bottom plot is at a tread trough, and the middle plot is midway between. The constant lines correspond to the initial and final values in each plot.
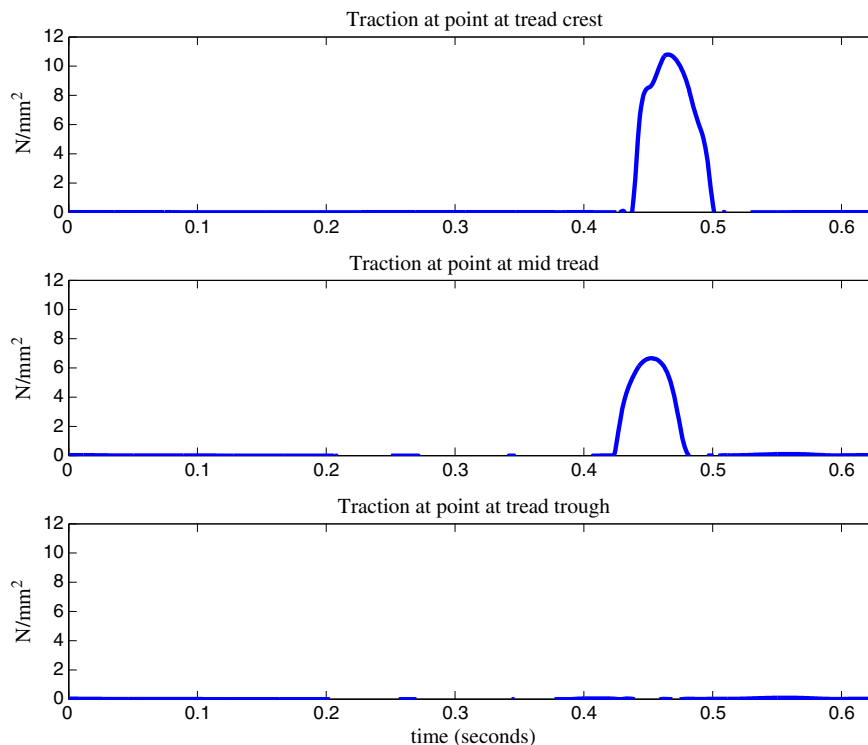
Figure 8. Plots of traction over one revolution. The plots represent points at different locations along the edge of the body. The top plot is at a tread peak, the bottom plot is at a tread trough, and the middle plot is midway between.

Using eight processors, method (1) takes less than 2 s to complete. This is far faster than method (2) and our method (3) due to the time independence of the problem. In particular, method (1) requires only a handful of linear solves for Newton's method to converge to the solution as opposed to the 10,000 time steps required to rotate the body in method (2) only 1/8th of a revolution. For method (3), the number of time steps required for one pass scales linearly with the arbitrarily chosen T. Thus, comparing method (3) to (1) on an axisymmetric body is not so meaningful.

Concentrating on method (2), however, allows us to make a better comparison. Method (2) requires approximately 20 full revolutions to reduce the L^2 norm of the residual vector below 10^{-4} when the viscoelastic relaxation parameter τ is 0.015 s. Each revolution take about 160 min to compute on eight processors, the entire solve takes about 53 h. Method (3) requires the equivalent of about 10 revolutions to achieve the same error, which is made up of a combination of evolutions of the full equations of motion and evolution of the linear equations of motion over the period T. This amounts to about 27 h, a 50% reduction in computational time.

Figure 10 shows the error in the methods as a function of the number of actual (or effective) revolutions of the body – a proxy for computational time. In the case of method (3), we count an effective revolution as being equivalent to time integrating our equations from $t = 0$ to T a total of eight times (based on our choice of T). We note that while our method converges faster than method (2), the best method for this range of parameters would be a hybrid: Method (2) performs better when we are far from the solution while our method is initially inefficient but eventually locks onto a faster convergence rate. Our method would converge quadratically if the GMRES tolerance were reduced more aggressively as a function of the residual in Newton's method, but this requires more iterations of the Krylov solver in later stages of Newton's method; see [26–28]. We also note that the convergence of both methods is closely related to the viscoelastic relaxation time parameter τ: larger values of τ lead to longer convergence times, which we can see by comparing the convergence rates for the different colored plots in Figure 10. With small values of τ (e.g. $\tau < 10^{-3}$), convergence can
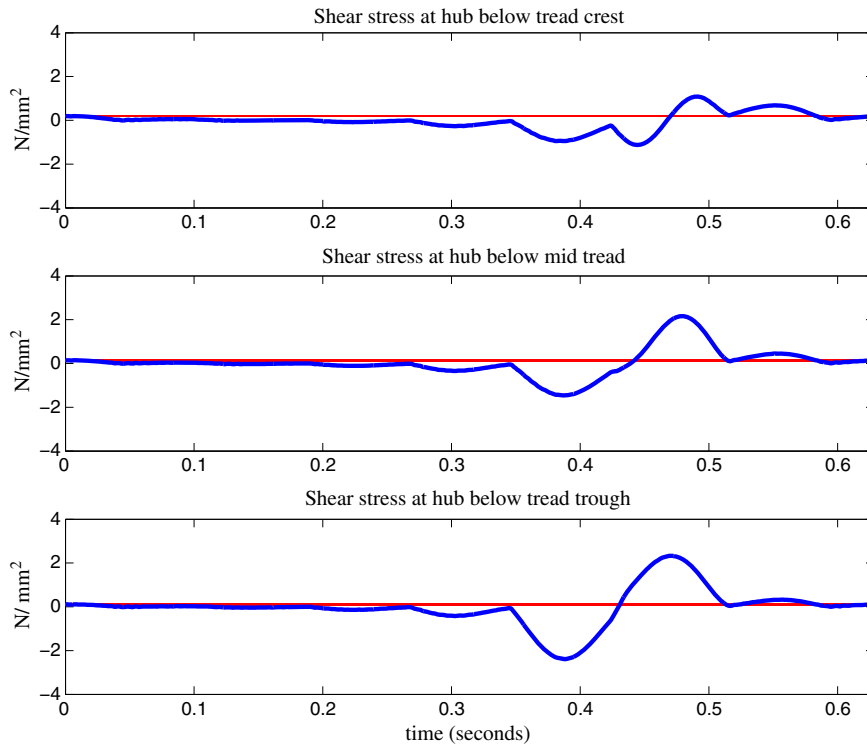
Figure 9. Plots of shear stresses of material points along the hub over one revolution. The plots represent points at different locations along the hub. The top plot is radially in line with a tread peak, the bottom plot with a tread trough, and the middle plot is midway between. The constant lines indicate the initial and final values, which are equal because of time-periodicity.
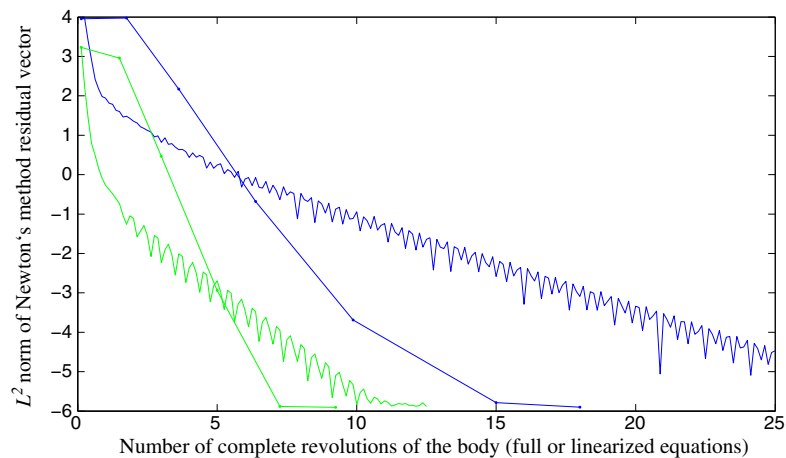

Figure 10. The smooth lines shows the error of the method presented in this paper (3), while the jagged lines shows the error of method (2). Blue (the more slowly converging case) corresponds to a relaxation time of $\tau = 0.015$ s, while green (the more quickly converging case) corresponds to $\tau = 0.01$ s.

happen in only a few revolutions, and there is little advantage in using method (3) over method (2). As τ becomes larger, the number of revolutions required for method (2) to converge grows faster than the number of Krylov solves needed in method (3), and our method converges faster. It should be pointed out that the relaxation times shown are rather small for common elastomeric materials, and thus, we are showing method (2) in its best light – especially when one considers that the ratio $(2\pi/\omega)/\tau$ is close to 50.

Finally, we note that the main computational expense of method (2) and method (3) is the time stepping computation. Because any time stepping algorithm, finite element discretization, or parallelization can be applied to both of the methods, the performance ratio of the two methods is independent of these choices.

5.5. A rotating viscoelastic oval

We now consider an example where the numerical method for finding cyclic steady states can capture the natural damped oscillations of a viscoelastic body. This demonstrates that the cyclic steady-state framework can accurately capture motions that would not be present in any steady-state calculation.

Consider a rotating oval-shaped body, which is modeled in our framework by setting $\beta = 2, \varepsilon = 0.4$. The oval is spun at 20 rad/s and can collide with a roadway (a flat surface), which we expect
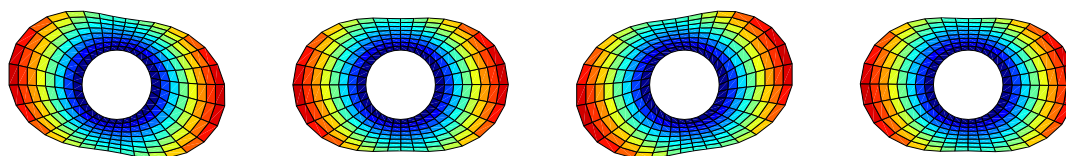

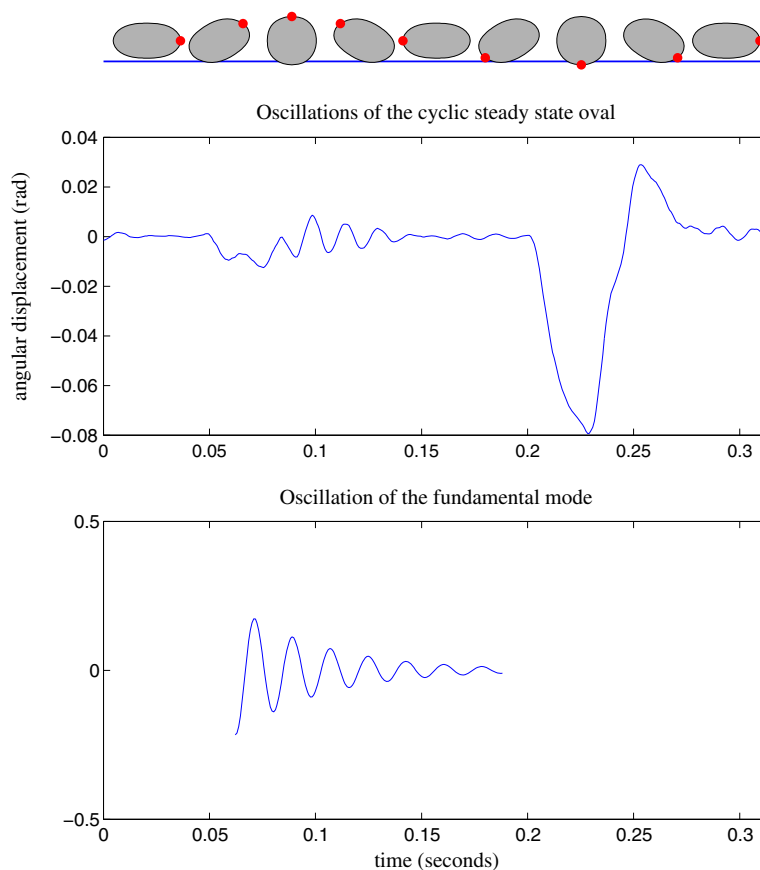Figure 11. Plots of a simple oscillating mode of the oval over one period.

Figure 12. Cyclic steady-state transient oscillations in a viscoelastic oval. (top) Schematic figures showing the position of the oval and its right-most tip. (middle) Plots of displacement $(\theta - \omega t)$ over a full revolution of the oval, where θ is the angular position of the right-most tip. (bottom) Plot of Re $(e^{\lambda t})$, where λ is the eigenvalue corresponding to the fundamental mode. The similar frequency and rate of decay of the two plots near 0.1 s indicate that the excitation of the fundamental mode is captured in the middle plot.
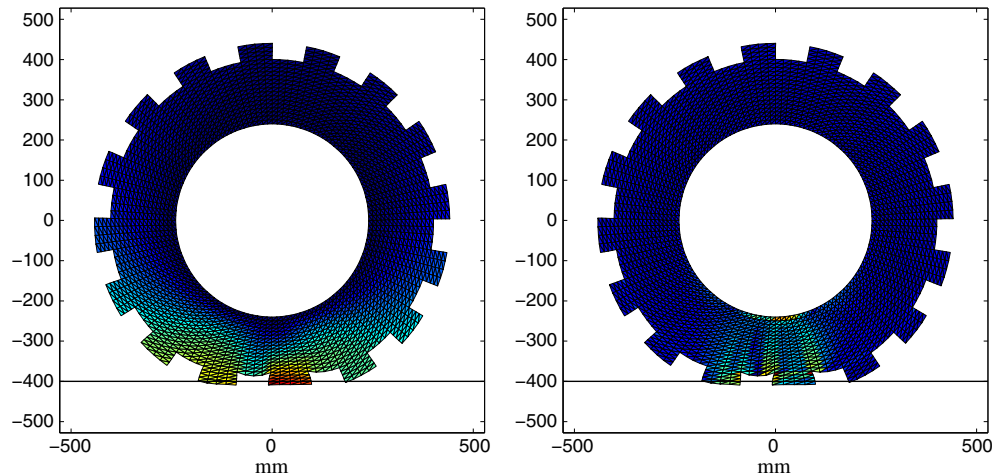
Figure 13. Cyclic steady state of a body with non-smooth treads. The coloring shows: (left) the magnitude of the displacement from the stress-free configuration; (right) the principal stress.

to excite vibrations. By computing the smallest eigenvalue and corresponding eigenvector of the tangent operator for the stationary oval, we observe the fundamental mode (Figure 11), which has a period of oscillation of approximately 1.7×10^{-2} s.

We compute a cyclic steady-state solution for half a revolution of the oval, which has a half-period of approximately 0.15 s. This is ample time to observe oscillations of the fundamental mode. The computed cyclic steady-state solution shows that the fundamental mode is excited as the oval contacts the road. In Figure 12, we see good agreement between the angular displacement of the computed cyclic steady state of the oval and the oscillations predicted by the fundamental mode analysis. In the middle plot, the oscillation near 0.05–0.15 s corresponds to the opposite end (left-most tip) of the oval contacting the road. The large displacement near 0.2–0.27 s corresponds to the right-most tip itself contacting the road.

5.6. Non-smooth tread patterns

Real automobile tires have complex tread patterns designed to maintain traction in rain, snow, and ice. Such treads are not as smooth as the sinusoidal perturbations of a cylinder studied previously. In this section, we confirm that the methodology developed in this paper can handle non-smooth tread blocks as well as low-order elements. Figure 13 shows the cyclic steady-state solution of a square-wave perturbation of a cylinder computed using continuous bi-linear quadrilateral elements (note that for plotting purposes the elements are shown with diagonals; this is only for plotting). The mesh consists of an inner cylinder, with 128 nodes in the circumferential direction and 17 nodes in the radial direction, together with 16 tread blocks, each containing a 5×5 array of nodes. The mesh spacing is uniform in the radial direction, and uniform with respect to polar angle in the circumferential direction. The behavior of the Newton–Krylov algorithm in this example is very similar to what was described in Section 5.2, with five Newton iterations consisting of 12 GMRES cycles being sufficient to reduce the L^2 norm of the residual by a factor of 10^{-9}. Thus, convergence of the Newton–Krylov scheme does not appear to suffer when the boundary is not smooth and lower-order elements are used to model the material. Although not shown, we have verified that our method (3) outperforms method (2) on this problem in a similar manner as to what was shown in Section 5.4.

6. CONCLUSION

The analysis of spinning and rolling non-axisymmetric bodies undergoing finite deformation has been a long-standing computational problem. In this work, we have outlined a scheme for computing

their cyclic steady states that does not involve rolling the body in a Lagrangian frame from zero velocity to its final speed and then waiting for it to settle into a cyclic steady state. The central idea was to note that the essence of the question is to determine an *initial condition* of the body that results in a time-evolved state at the end of a (fixed) period, which is identical to the initial condition. This permits one to construct a residual expression that must be zero for a cyclic steady state. The zero of this residual is then found under the constraint of the partial differential equations that govern the time evolution of the rotating body's motion and internal state variables. The scheme has been demonstrated on a set of simple examples in order to illustrate its viability and to highlight the types of technical response quantities that can be computed from such a methodology. The method is also seen to outperform the naïve method of simply rolling the body from a static state to the rolling velocity.

APPENDIX A: LINEARIZATIONS

Recall the linearized equations:

$$
\begin{aligned}
\int_{\mathcal{B}} \dot{\widehat{\boldsymbol{\phi}}} \cdot \zeta &= \int_{\mathcal{B}} \widehat{\boldsymbol{v}} \cdot \zeta \\
\int_{\mathcal{B}} \dot{\widehat{\boldsymbol{v}}} \cdot \eta &= \int_{\mathcal{B}} -\frac{1}{\rho_R} \widehat{\mathbf{P}} : D\eta + \int_{\Gamma_e} \frac{1}{\rho_r} \widehat{\mathbf{h}} \cdot \eta \\
\int_{\mathcal{B}} \dot{\widehat{\mathbf{b}}}_e : K &= \int_{\mathcal{B}} \left(\widehat{\boldsymbol{\ell} \mathbf{b}_e} + \widehat{\mathbf{b}_e \boldsymbol{\ell}^{\mathrm{T}}} - 2\widehat{\mathcal{V}(\boldsymbol{\tau}_v)\mathbf{b}_e} \right) : K .
\end{aligned}
\tag{A.1}
$$

We need formulas for $\widehat{\mathbf{P}}, \widehat{\mathbf{h}}$, and $\dot{\widehat{\mathbf{b}}}_e$. This requires a series of computations. The first set culminates in the computation of $\widehat{\mathbf{P}}_e$:

$$
\begin{aligned}
\widehat{\mathbf{F}} &= D\widehat{\boldsymbol{\phi}} \\
\widehat{\mathbf{C}} &= \widehat{\mathbf{F}}^{\mathrm{T}}\mathbf{F} + \mathbf{F}^{\mathrm{T}}\widehat{\mathbf{F}} \\
\widehat{I}_1 &= 2\left(\mathbf{F} : \widehat{\mathbf{F}} \right) \\
\widehat{I}_3 &= 2I_3 \left(\mathbf{F}^{-\mathrm{T}} : \widehat{\mathbf{F}} \right) \\
\widehat{\mathbf{F}^{-\mathrm{T}}} &= -\mathbf{F}^{-\mathrm{T}}\widehat{\mathbf{F}}^{\mathrm{T}}\mathbf{F}^{-\mathrm{T}} \\
\widehat{\mathbf{P}}_e &= \frac{\kappa}{2} \left(\widehat{I}_3\mathbf{F}^{-\mathrm{T}} + (I_3 - 1)\widehat{\mathbf{F}^{-\mathrm{T}}} \right) \\
&\quad + \mu(1-s)\left(\widehat{\mathbf{F}} - \widehat{\mathbf{F}^{-\mathrm{T}}} \right) + \mu s \left(\widehat{I}_1\mathbf{F} + I_1\widehat{\mathbf{F}} - \left(\mathbf{F}\widehat{\mathbf{C}} + \widehat{\mathbf{F}}\mathbf{C} \right) - 2\widehat{\mathbf{F}^{-\mathrm{T}}} \right) .
\end{aligned}
$$

The second set gives $\widehat{\mathbf{P}_v}$:

$$
\begin{aligned}
\widehat{I}_1^e &= \left(\widehat{\mathbf{b}}_e : \mathbf{I} \right) \\
\widehat{I}_3^e &= I_3^e \left(\mathbf{b}_e^{-1} : \widehat{\mathbf{b}}_e \right) \\
\widehat{\boldsymbol{\tau}_v} &= \nu \left(\frac{\kappa}{2}\widehat{I}_3\mathbf{I} + \mu(1-s)\widehat{\mathbf{b}}_e + \mu s \left(\widehat{I}_1^e\mathbf{b}_e + I_1^e\widehat{\mathbf{b}}_e - \left(\mathbf{b}_e\widehat{\mathbf{b}}_e + \widehat{\mathbf{b}}_e\mathbf{b}_e \right) \right) \right) \\
\widehat{\mathbf{P}_v} &= \boldsymbol{\tau}_v\widehat{\mathbf{F}^{-\mathrm{T}}} + \widehat{\boldsymbol{\tau}_v}\mathbf{F}^{-\mathrm{T}} .
\end{aligned}
$$

$\widehat{\mathbf{P}}$ is then given by

$$
\widehat{\mathbf{P}} = \widehat{\mathbf{P}}_e + \widehat{\mathbf{P}_v} .
$$

A third set of computations leads to $\dot{\widehat{\mathbf{b}}}_e$:

$$
\dot{\widehat{\mathbf{F}}} = D\widehat{\boldsymbol{v}}
$$

$$
\widehat{\boldsymbol{\ell}} = \dot{\widehat{\mathbf{F}}}\mathbf{F}^{-1} + \dot{\mathbf{F}}\widehat{\mathbf{F}^{-1}}
$$

$$
\widehat{\mathcal{V}(\boldsymbol{\tau}_v)} = \frac{1}{2\mu\tau}\left(\widehat{\boldsymbol{\tau}_v} - \frac{1}{2}\left(\operatorname{tr}\widehat{\boldsymbol{\tau}_v}\right)\mathbf{I}\right) + \frac{1}{4\kappa\tau}\left(\operatorname{tr}\widehat{\boldsymbol{\tau}_v}\right)\mathbf{I}
$$

$$
\dot{\widehat{\mathbf{b}}}_e = \widehat{\boldsymbol{\ell}\mathbf{b}_e} + \widehat{\mathbf{b}_e\boldsymbol{\ell}^{\mathrm{T}}} - 2\widehat{\mathcal{V}(\boldsymbol{\tau}_v)\mathbf{b}_e}
$$

$$
= \left(\widehat{\boldsymbol{\ell}}\mathbf{b}_e + \boldsymbol{\ell}\widehat{\mathbf{b}_e}\right) + \left(\widehat{\mathbf{b}_e}\boldsymbol{\ell}^{\mathrm{T}} + \mathbf{b}_e\widehat{\boldsymbol{\ell}^{\mathrm{T}}}\right) - 2\left(\widehat{\mathcal{V}(\boldsymbol{\tau}_v)}\mathbf{b}_e + \mathcal{V}(\boldsymbol{\tau}_v)\widehat{\mathbf{b}_e}\right).
$$

Finally, we compute $\widehat{\mathbf{h}}$:

$$
\widehat{x_2} = \widehat{\boldsymbol{\phi}_2}
$$

$$
\widehat{\mathbf{h}} = -k\gamma'(-h - x_2)\widehat{x_2}\mathbf{e}_2.
$$

REFERENCES

1. Padovan J, Paramodilok O. Generalized solution of time dependent traveling load problem via moving finite element scheme. *Journal of Sound and Vibration* 1983; **91**:195–209.
2. Padovan J, Paramodilok O. Transient and steady state viscoelastic rolling contact. *Computers and Structures* 1985; **20**:545–553.
3. Oden JT, Lin R. On the general rolling contact problem for finite deformations of a viscoelastic cylinder. *Computer Methods in Applied Mechanics and Engineering* 1986; **57**:297–367.
4. Padovan J. Finite element analysis of steady and transiently moving/rolling nonlinear viscoelastic structure – I. Theory. *Computers and Structures* 1987; **27**:249–257.
5. Bass JM. Three-dimensional finite deformation, rolling contact of a hyperelastic cylinder: formulation of the problem and computational results. *Computers and Structures* 1987; **26**:991–1004.
6. Kennedy R, Padovan J. Finite element analysis of steady and transiently moving/rolling nonlinear viscoelastic structure – II. Shell and three-dimensional simulations. *Computers and Structures* 1987; **27**:249–257.
7. Le Tallec P, Rahier C. Numerical models of steady rolling for non-linear viscoelastic structures in finite deformations. *International Journal for Numerical Methods in Engineering* 1994; **37**:1159–1186.
8. Govindjee S, Mihalic PA. Viscoelastic constitutive relations for the steady spinning of a cylinder. *Technical Report UCB/SEMM-98/02*, University of California Berkeley, Department of Civil Engineering, 1998.
9. Qi J, Herron JR, Sansalone KH, Mars WV, Du ZZ, Snyman M, Surendranath H. Validation of a steady-state transport analysis for rolling treaded tires. *Tire Science and Technology (TSTCA)* 2007; **35**:183–208.
10. Ciarlet PG. *Mathematical Elasticity*. Elsevier: North-Holland, 1988.
11. Ball JM. Convexity conditions and existence theorems in nonlinear elasticity. *Archives for Rational Mechanics and Analysis* 1977; **63**:337–403.
12. Potter T. Dynamics and stability of rolling viscoelastic tires. *Ph.D. Thesis*, University of California, Berkeley, 2013.
13. Simo JC. On a fully three-dimensional finite-strain viscoelastic damage model: formulation and computational aspects. *Computer Methods in Applied Mechanics and Engineering* 1987; **60**:153–173.
14. Govindjee S, Potter T, Wilkening J. Dynamic stability of spinning viscoelastic cylinders at finite deformation 2014. (in submission).
15. Govindjee S, Reese S. A presentation and comparison of two large deformation viscoelastic models. *ASME Journal of Engineering Materials and Technology* 1997; **119**:251–255.
16. Reese S, Govindjee S. A theory of finite viscoelasticity and numerical aspects. *International Journal of Solids and Structures* 1998; **35**:3455–3482.
17. Reese S, Govindjee S. Theoretical and numerical aspects in the thermo-viscoelastic material behaviour of rubber-like polymers. *Mechanics of Time-Dependent Materials* 1998; **1**:357–396.

18. Sidoroff F. Un modèle viscoélastique non linéaire avec configuration intermédiaire. *Journal de Mécanique* 1974; **13**:679–713.
19. Viswanath D. Recurrent motions within plane Couette turbulence. *Journal of Fluid Mechanics* 2007; **580**:339–358.
20. Ambrose DM, Wilkening J. Computation of time-periodic solutions of the Benjamin–Ono equation. *Journal of Nonlinear Science* 2010; **20**:277–308.
21. Williams MO, Wilkening J, Shlizerman E, Kutz JN. Continuation of periodic solutions in the waveguide array mode-locked laser. *Physica D* 2011; **240**:1791–1804.
22. Wilkening J, Yu J. Overdetermined shooting methods for computing standing water waves with spectral accuracy. *Computational Science & Discovery* 2012; **5**:014017 (38pp).
23. Hairer E, Nørsett SP, Wanner G. *Solving Ordinary Differential Equations I*, Nonstiff Problems. Springer-Verlag: Berlin, 1987.
24. Dormand JR, Prince PJ. A family of embedded Runge-Kutta formulae. *Journal of Computational and Applid Mathematics* 1980; **6**:19–26.
25. Dormand JR, Prince PJ. Practical Runge-Kutta processes. *SIAM Journal on Scientific and Statistical Computing* 1989; **10**:977–989.
26. Knoll DA, Keyes DE. Jacobian-free Newton–Krylov methods: a survey of approaches and applications. *Journal of Computational Physics* 2004; **193**:357–397.
27. Dembo RS, Eisenstat SC, Steihaug T. Inexact Newton methods. *SIAM Journal on Numerical Analysis* 1982; **19**: 400–408.
28. Eisenstat SC, Walker HF. Choosing the forcing terms in an inexact Newton method. *SIAM Journal on Scientific Computing* 1996; **17**:16–32.